HHS Public Access

Author manuscript

J Alzheimers Dis. Author manuscript; available in PMC 2018 March 13.

Published in final edited form as:

J Alzheimers Dis. 2017 ; 55(2): 797–811. doi:10.3233/JAD-160289.

Aerosol Delivery of Curcumin Reduced Amyloid-β Deposition and Improved Cognitive Performance in a Transgenic Model of Alzheimer's Disease

Richard McClure[a,b,h], **Henry Ong**[a,b], **Vaibhab Janve**[a,b], **Shawn Barton**[a,b], **Meiying Zhu**[a,b], **Bo Li**[a,b], **Mary Dawes**[f], **W. Gray Jerome**[g], **Adam Anderson**[a,b,c], **Pierre Massion**[d], **John C. Gore**[a,b,c,h], and **Wellington Pham**[a,b,c,d,e,h,*]

[a]Institute of Imaging Science, Vanderbilt University, Nashville, TN, USA

[b]Department of Radiology and Radiological Sciences, Vanderbilt University, Nashville, TN, USA

[c]Department of Biomedical Engineering, Vanderbilt University, Nashville, TN, USA

[d]Vanderbilt Ingram Cancer Center, Vanderbilt University, Nashville, TN, USA

[e]Vanderbilt Institute of Chemical Biology, Nashville, TN, USA

[f]Vanderbilt Cell Imaging Core Laboratory, Nashville, TN, USA

[g]Department of Pathology, Microbiology and Immunology, Vanderbilt University, Nashville, TN, USA

[h]Vanderbilt Brain Institute, Vanderbilt University, Nashville, TN, USA

Abstract

We report a novel approach for the delivery of curcumin to the brain via inhalation of the aerosol for the potential treatment of Alzheimer's disease. The percentage of plaque fraction in the subiculum and hippocampus reduced significantly when young 5XFAD mice were treated with inhalable curcumin over an extended period of time compared to age-matched nontreated counterparts. Further, treated animals demonstrated remarkably improved overall cognitive function, no registered systemic or pulmonary toxicity associated with inhalable curcumin observed during the course of this work.

Keywords

Aerosol; amyloid-β; curcumin; nebulization

*Correspondence to: Wellington Pham, PhD, Associate Professor of Radiology, Associate Professor of Biomedical Engineering, Institute of Imaging Science, Vanderbilt University School of Medicine, 1161, 21st Avenue South, Nashville, TN 37232-2310, USA. Tel.: +1 615 936 7621; wellington.pham@vanderbilt.edu.

Authors' disclosures available online (http://j-alz.com/manuscript-disclosures/16-0289r1).

SUPPLEMENTARY MATERIAL

The supplementary material is available in the electronic version of this article: http://dx.doi.org/10.3233/JAD-160289.

INTRODUCTION

Alzheimer's disease (AD) is among the very few illnesses that has been known for over a century but continue to impact millions of people worldwide in an unabated manner. AD is the most common cause of dementia among elderly people [1]. The epidemic threat of AD is particularly worrisome in an aging population because no disease-modifying therapies are available. The mechanism that regulates neuronal degeneration in AD remains unknown; however, the cytopathologic hallmarks of the disease appear to be the formation of soluble amyloid-β proteins (Aβ), which cluster into Aβ oligomers and polymers. As the size of the aggregates increases, they may precipitate as insoluble amyloid fibrils, in which the structure is stabilized into plaques between the neurons, leading ultimately to profound neuron toxicity [2, 3]. Thus, according to this amyloid cascade hypothesis of AD pathogenesis, interruption of any of the steps that lead to amyloid plaque aggregation could potentially lead to an efficacious treatment. Unfortunately, preclinical and clinical AD trials seeking to evaluate the therapeutic validity of the Aβ cascade hypothesis have not been particularly successful. However, the failure of those trials may be attributed to their inappropriate designs rather than to a weakness in the amyloid concept. First of all, data obtained from those clinical studies suggested that clinical failures occurred because there was poor bioavailability of the drugs at the target site due to lack of penetration of the blood-brain barrier (BBB) [4]. Second, it is worth mentioning the critical challenge in recruiting and classifying patients with different AD pathological stages. Moderate to full-blown AD exudes copious amounts of Aβ, which causes havoc among neurons and possibly tissue atrophy. At this stage, therefore, removing Aβ or inhibiting its aggregation is likely futile.

To address the limitation of delivering AD therapeutics that cross the BBB, we developed an aerosol-based technique capable of delivering robust amounts of compounds to the brain. As we show herein, the technique offers a far safer translation to clinical use than conventional methods. In particular, drugs intended for the brain have amphiphilic properties making them incompatible with conventional formulations intended for intravenous (I.V.) injection and thus necessitating the use of non-biological solvents that have considerable toxicity. From the drug delivery perspective for AD, the intrinsic advantage of using an aerosolized drug formulation is that the inhaled materials enter the lungs and they are mixed with blood in the circulatory system, but will not experience the first-pass effect, so that hepatotoxicity is not concerned. Further, this route of distribution also reduces drug degradation by the hepatic P450 family of enzymes. More intriguingly, a secondary distribution route for aerosols, largely unavailable with other techniques, exists in the direct nasal pathway followed by drug absorption via the olfactory epithelium network. The neural connection between the nasal cavity and the brain offers a unique opportunity to deliver drugs noninvasively, without the need to modify chemical structures. Further, this pathway not only allows drugs incapable of crossing the BBB to enter the central nervous system, but also eliminates the need for systemic delivery, thereby reducing unwanted systemic side effects [5, 6].

Here, we demonstrate a unique application approach that utilizes aerosol-mediated drug delivery to recapitulate the therapeutic benefits of curcumin for the treatment of AD. Curcumin is a natural product found in turmeric, which is a key ingredient in curry powder

(Fig. 1A). This compound has been subjected to intense study during the past several decades for a number of disease models including inflammation [7–12] and cancer [13–19] as well as for neurodegenerative disorders [20–23]. As with any amphiphilic molecule intended for the brain, the formulation designed of curcumin for *in vivo* study is challenging, particularly because it has poor aqueous solubility, which thus represents a major hurdle for achieving adequate I.V. administration. Curcumin is soluble in organic solvents with low molar extinction coefficients, which renders it unsuitable for use in translational work. Traditionally, solubility issues such as this have been overcome via the addition of a high concentration of a detergent-like solution in the formulation buffer. However, experiences gained from animal studies conducted in our laboratory showed that acute lethality is high due to the occlusions caused by the resulting viscous solution. The solubility problem is further exacerbated because of curcumin's poor absorption in the intestinal lining.

MATERIALS AND METHODS

Thioflavin T and tween-20 were obtained from Sigma-Aldrich. All reagents were used without further purification. 4G8 anti-Aβ monoclonal antibodies (Covance, Princeton, NJ) and peroxidase conjugated secondary antibodies were obtained from Covance (Princeton, NJ) and (Pierce, Rockford, IL) and used under companies' recommendation. Immunohistochemical staining and western blot analyses were performed using the avidin-biotin peroxidase complex method available in a commercial kit (Mouse IgG Vectastain ABC Elite kit, Vector Laboratories).

Animals

The C57BL/6 and 5XFAD mice were maintained at Vanderbilt University under standard conditions, in a 12-h light/dark cycle and with free access to food and water. The 5XFAD mice over express both mutant human APP and PS1 express high APP levels correlating with high burden and accelerated accumulation of the Aβ. A colony of 5XFAD transgenic mice obtained from Jackson Laboratories was maintained by crossing 5XFAD mice with a wild-type (wt) C57BL/6J strain. The mice were genotyped by a standard polymerase chain reaction using DNA isolated from tail tips with the following primers: PSEN1 forward, 5′-TCATGACTATCCTCCTGGTGG3′and reverse, 5′-CGTTATAGGTTTTAAACACTTCCCC-3′. For APP, forward, 5′-AGGACTGACCACTCGACCAG-3′and reverse, 5′-CGGGGGTCTAGTTCTGCAT-3′. We also genotyped mice for the presence of retinal degeneration Pde6b^{rd1} mutation using forward, 5′-AAGCTAGCTGCAGTAACGCCATTT-3′and reverse, 5′-ACCTGCATGTGAACCCAG-TATTCTATC-3′. After polymerase chain reaction amplification, the DNA product of each reaction was analyzed by size fractionation through a 1% agarose gel; with Pde6b mutant = 560 bp, APP transgene = 377 bp and PSEN1 transgene = 608 bp. The 5XFAD mice were maintained as homozygous. Animal experiments were conducted per the guidelines established by Vanderbilt University's Institutional Animal Care and Use Committee. At the end of the study, animals were euthanized by cervical dislocation after sedated with isoflurane. Clinical signs were used to check after animal euthanasia including heartbeats, toe-pinching for reflection. Further, if animals show signs of illness (weight loss, food withdrawal, or infection) they will be

sacrificed before the endpoints. All experimental procedures in this study were approved by the Vanderbilt University IACUC panel.

qPCR

Total RNA was extracted from a mouse's brain using the TRIzol reagent. The tissue was homogenized in 1 ml of TRIzol reagent per 100 mg of tissue. Then, reverse transcription reaction was performed using iScript cDNA Synthesis Kit (Bio-RAD). Quantitative real-time PCR analysis of AZ mouse COX-2 using the forward primer 5′-AGAAGGAAATGGCTGCAGAA-3′and the reverse primer 5′–GCTCGGCTTCCAGTATTGAG-3′. Control wt using a B-actin forward primer 5′–TTCTTTGCAGCTCCTTCGTTGCCG-3′ and the reverse primer 5′–TGGATGGCTACGTACATGG-CTGGG-3′ The COX -2 mRNA level was quantified by qRT-PCR using the iQ SYBR supermix (BIO-RAD). Relative quantification normalized to a reference gene.

Curcumin aerosol formulation and administration

Curcumin powder was added gradually to a mixture of PBS (1×, pH 7.4) and tween-20 (10%) at a ratio of 5:1 (v/v) under vigorous stirring until the concentration reached 7 mg/mL. The mixture was further heated up to 70°C to facilitate the solubility. The cloudy solution was then sonicated for 30 min or until a clear solution is obtained. The curcumin aerosol quality was determined by collecting the aerosol trapped in the filter sampler using HPLC. Aside from the authentic curcumin peak on the HPLC, the data demonstrated that no extra peak was present, which suggested that the formulation was stable.

During animal trials, non-anesthetized mice were placed into a restraining tube that was inserted into the exposure chamber. The animal's snout was secured within the restraint tube by a stainless steel nose cone, which focused delivery of the aerosol to the breathing zone of the animal. The tapered nose cone inside the restraint tube enables the animal to inhale the aerosol. Approximately 2 h was required for each treatment of a dose of 5 mg/Kg. It is noteworthy that no animals died prior to the experimental endpoint while treating them with inhalable curcumin.

Y-maze study

In an effort to quantitatively assess the effect of inhaled curcumin on spatial-dependent and working memory in a pre-clinical mouse model of AD, the Y-maze behavioral assay was employed. Briefly, 6-week old 5XFAD mice ($n = 10$) were chronically administered a 5 mg/kg dose of nebulized curcumin three times a week for 18 weeks. Two cohorts consisting of a group of age-matched 5XFAD and a group of wt mice ($n = 10$ per group), which remained in their home caging and were untreated throughout the study served as controls. Following a one-week habituation period in the behavioral testing facility to decrease experimental confounds attributable to the animals' stress, working memory and spatial memory were assessed via Y-maze. All behavioral assays were run during the night cycle and all mice were allowed to habituate to the experimental environment for 3 h prior to testing.

Working memory Y-maze paradigm

In this behavioral assay, spontaneous alteration was tested in a Y-shaped maze with three opaque plastic arms at a 120° angle from each other. In an effort to make each arm distinguishable to the animal, laminated sheets of uniquely patterned paper were fastened to the outside of the maze. These patterns included a “black arm” surrounded completely with black background while a “dotted arm” consisted of alternating black and white vertical bars with a 2.5 cm width. Lastly, the third arm or “dotted arm” contained white circles with a 2 cm diameter on a black background. Prior to behavioral testing, rigorous controls were run on a naïve cohort of animals to insure no intrinsic preference for a particular arm existed. The entire maze was cleaned and dried thoroughly with ethanol both before and after each trial to insure standardized maze conditions. After introduction of the mouse into a standardized arm of the maze, the animal was allowed to freely explore the three arms for 6 min with the sequence of arm entries being recorded. The number of arm entries and the number of correct triads were recorded using ANY-maze behavior tracking software in conjunction with a CCD video camera system. Arm entries were logged when all four limbs of the animal crossed a line arbitrarily placed 50% down each of the three maze arms. A quantitative evaluation of working memory performance was made by calculating the percent spontaneous alteration for each animal. Possible confounds associated with differences in locomotion between cohorts were controlled for via comparison of the total number of arm entries.

Spatial-memory dependent Y-maze behavioral assay

One week following completion of the working memory Y-maze behavioral assay, all animal cohorts were then tested in the spatial memory paradigm. To directly assess hippocampal function at the behavioral level, a two-phase Y-maze paradigm was employed. As in the working memory task, each arm of the Y-maze was decorated with spatial cues to increase the salience of each arm. Notably, quantification of the mean number of entries and seconds exploring each arm of the maze in a naïve cohort of animals confirmed no innate preference for any of the arms. Additionally, no differences in the initiative to explore were noted between any of the cohorts suggesting that any observed differences in behavior truly reflect alterations in spatial memory. During the first phase of this paradigm, the mouse was allowed to freely explore two of the three arms of the Y-maze for a 6-min period. The arm, which was blocked during this first phase was randomized between animals, and designated as the “novel” arm in the secondary phase of the study. Following the first period of exploration, each mouse was returned to its home cage and left undisturbed for a 30-min period. Following this period of rest, each mouse was placed into a randomized arm of the maze and allowed to freely explore all three arms of the Y-maze for a 5-min interval. To quantitatively assess spatial memory, the proportion of time spent exploring the previously blocked “novel arm” arm was quantified and plotted as the fraction of overall time spent exploring. All arms of the maze were cleaned with 70% ethanol both prior to and after each trial to insure standardized maze conditions between animals.

Tissue preservation and thioflavin staining

Following cardiac-perfusion as described in the corresponding methods section, the extracted brain tissue was fixed first 4% PFA, then in a 10% sucrose/PBS solution for 5 and 2 days, respectively. Immediately after fixation, each brain tissue ($n = 5$ per group) was divided along the sagittal fissure. One hemisphere was then utilized for western blot analysis as described elsewhere while the other hemisphere was utilized for histochemical staining using thioflavin. Sagittal sections (12 mm) were mounted onto charged glass slides, placed in 4% PFA for 10 min, transferred to TRIS buffer (20 mM TRIS, 25 mM NaCl, and 1 mM $MgCl_2$) for 5 min. Treated sections were then incubated for 30 min at 37°C with a freshly prepared 1% thioflavin solution which was sonicated and passed through a 0.2 micron syringe filter prior to use. Following PBS washes, dehydration in a series of alcohols (ranging from 95–100% ethanol), and clearance in xylene, each slide was then cover-slipped using VECTASHEILD mounting medium (Vector Laboratories Inc., Burlingame CA, USA).

Assessment of Aβ plaque burden by thioflavin histochemical staining

To quantitatively assess the effect of chronic curcumin therapy on Aβ plaque burden in the brain, sagittal sections ($n = 50$) isolated from nebulized 5XFAD mice and untreated littermates ($n = 5$ per group) were stained with 1% thioflavin T as described. Fluorescence imaging of the hippocampus, subiculum, and neocortex were then acquired in the GFP channel. Automated quantification of Aβ plaque burden was performed for each slide using a custom image analysis script written in MATLAB (Mathworks, Natick, MA). In more detail, first, uneven background illumination is removed using morphological top-hat filtering. Second, the image contrast was enhanced to highlight plaques by nonlinear mapping. Third, a plaque mask was created using a user-defined spatially varying threshold based on the background illumination, which was then cleaned up using a morphological opening. Finally, manual regions-of-interest (ROIs) were drawn around the hippocampus and subiculum and were selected to avoid histological artifacts. From the ROI plaque masks, plaque morphologic parameters can be calculated. Plaque density is reported in mm^{-2} and is defined as the number of plaques divided by the ROI area.

Assessment of Aβ plaque burden by stereological measurement

Images were captured using a high throughput Leica SCN400 Slide Scanner automated digital image system from Leica Microsystems. Whole slides were imaged at 20× magnification to a resolution of 0.5μm/pixel. Images were processed in Matlab (Mathworks, Inc. Natick, MA) using a custom semi-automated analysis script to enhance plaque to tissue contrast and to mitigate any tissue processing artifacts. Specific steps include, removal of background illumination using top hat filter, image smoothing with median filter (21 pixel kernel used) to remove salt-pepper noise and extracting Red, Green, and Blue (RGB) channels from true color image. Blue channel displayed maximum contrast between plaques and surrounding tissue and was used to create a plaque mask based on region specific threshold. Hippocampus region including 3 mm cortex region was extracted from high-resolution images. The extracted images were subdivided into anatomical regions: dentate gyrus (DG), stratum (CA), subiculum (Sub), and cortex (CTX) using manually drawn ROIs based on Allen brain mouse atlas (http://mouse.brain-map.org/static/atlas). The ROIs were

then used to count plaques in each sub region by two independent observers to quantify the plaque burden. The plaques were verified manually based on morphological features on high-resolution tissue micrographs that differentiated plaques from nonspecific staining. The independently assessed plaque count from two observers matched closely and the average plaque counts were assigned to each region. A total of $n = 4$ control and $n = 6$ treated sections were processed in the same manner.

Transmission electron microscopy

Ultrastructural analysis of neurite diameter in the CA3 hippocampal region of 6-month-old 5XFAD mice was performed using TEM. Two cohorts of 5XFAD were analyzed. Representing the treatment group, 6-week-old 5XFAD mice were chronically administered a 5 mg/kg dose of aerosolized curcumin three times a week for 18 weeks ($n = 3$). As a control, untreated, sex-matched 6-month-old 5XFAD mice were employed ($n = 2$). Once of appropriate age, mice were perfused with 20 mL of a 0.1 M cacodylate/sucrose buffer to wash out extraneous proteins. Subsequently, cardiac perfusion with 2% PFA/2.5% glutaraldehyde in 0.1 M cacodylate/sucrose buffer was employed to fix the tissues for TEM analysis. Brains were next surgically harvested and placed in 2%PFA/2.5% glutaraldehyde in 0.1M cacodylate/sucrose buffer for 2 h at room temperature before being stored for 6 days overnight at 4°C. Using a scalpel, the hippocampal region of the brain was excised and subsequently rinsed in 0.1 M cacodylate buffer. The sample was then post-fixed with 1% osmium tetroxide in 0.1 M cacodylate buffer for 1 h at room temperature, then overnight in refrigerator. After rinsing in 0.1 M cacodylate buffer, the sample was dehydrate through a graded series of ethanol in 15-min intervals. Over the course of 3 days, the sample was embedded in TEM-compatible epoxy resin and then cut into thick sections (0.5μm) for analysis via light microscopy. This facilitated the identification of the CA3 sub-region, facilitating the shaving of ultrathin sections (70 nm) from the epoxy-embedded sample. Ultrathin sections were next post-stained with uranyl acetate for 15 min. These same samples were then subsequently stained with Reynolds lead citrate for 10 min. Lastly, each sample was examined by transmission electron microscopy (FEI Tecnai T-12 electron microscope) at 100 KeV.

Cardiac perfusion procedure and western blot

Treated and untreated mice were anesthetized with 3% isoflurane mixed with 2% oxygen before undergoing transcardiac perfusion. After a small thoracic cavity was generated using a sterilized scalpel to expose the heart, perfusion commenced with ice cold PBS that contained a protease inhibitor cocktail (Roche, Indianapolis, IN) (pH 7.4, 30 mL) using a 25-gauge needle inserted into the ventricle while the atrium was snipped off. Following perfusion, half of the brain was fixed with 4% PFA overnight at 4°C, then followed by a sucrose precipitation step. The brain was then embedded in OCT and stored at −80°C before use. The other half of the brain was prepared for western blot, in which the tissue was homogenized in 2 mL of tissue lysate buffer containing a protease inhibitor (Sigma-Aldrich, St. Louis, MO). The brain homogenates were normalized for protein content using BCA assay (Pierce, Rockford, IL), and 20μg of protein was run on 4–12% Tris-HCl SDS-PAGE gels (Bio-Rad, Hercules, CA). After transferred to polyvinylidene difluoride membrane, blots were incubated with 4G8 anti-Aβ monoclonal antibodies (Covance, Princeton, NJ) at

1:1000 overnight at 20°C. Peroxidase conjugated secondary antibodies (Pierce, Rockford, IL) were applied, and immunoblot signals were detected by enhanced chemiluminescence and quantified using the Xenogen IVIS 200 bioluminescent and fluorescent imaging system.

Lung toxicity analysis

To provide a preliminary assessment of pulmonic toxicity potentially attributable with curcumin inhalation, the lung tissue of acutely (n = 3) and chronically nebulized (n = 3) 6-month-old 5XFAD mice were examined by a blinded pathologist. The “acute nebulization” cohort received one standard 5 mg/kg dose of curcumin as previously described and were sacrificed 24 h post-exposure. In contrast, the “chronic nebulization” cohort received 48 of 5 mg/kg doses of inhaled curcumin over a 16-week time-period (3 doses/week). Just as in the acute nebulization cohort, mice in the chronically nebulized cohort received their last dose 24 h prior to sacrifice. Immediately prior to sacrifice, cardiac perfusion was performed under 2% isoflurane as previously described. The trachea and lung tissues were then surgically dissected as a complete unit, before being inflated with 10% formalin to facilitate observation of alveolar architecture. Briefly, following removal of the rib cage, forceps were utilized to separate the trachea and esophagus. Next a 26-gauge syringe containing 10% formalin was used to penetrate the trachea and inflate the lung lobes. The inflated tissues were fixed in 10% formalin for 2 days before serial sectioning/slide mounting at 8 microns. H&E and Masson Tri-chrome staining was performed on each tissue section, with >50 microns between each section to ensure adequate sampling of the lung tissue (n = 5 sections/mouse/stain). Both H&E and tri-chrome stained sections from each animal were reviewed by a blinded clinical pathologist for any pathological evidence of toxicity. Images used for quantitative analysis of collagen deposition were captured by traditional light microscopy methods (Visen FMT, PerkinElmer, MA, USA) at 10× & 20× magnification for respiratory bronchioles and lung parenchyma, respectively. Quantitative analysis of collagen deposition in the respiratory bronchioles (n = 20 per animal) and lung parenchyma (n = 30 ROI per animal) were performed in ImageJ on Masson’s tri-chrome stained lung tissue sections. Briefly, RGB stacks were generated from the original images and a uniform threshold applied to the red channel to facilitate isolation of the signal attributable to collagen. Next, ROIs were manually drawn by a blinded investigator. Lastly, the area fraction of lung tissue comprised of collagen was calculated as the quotient of red pixels over the total number of pixels in the ROI.

Blood chemistry toxicity analysis

To investigate the potential of systemic toxicity associated with curcumin administration, the blood serum of wt mice (n = 2/group) was analyzed following curcumin dosing via nebulization or tail-vein injection. Chemistry profiles (CPs) and complete blood counts (CBCs) from each treatment group were then compared to untreated littermates. The I.V. injected cohort received a 5 mg/kg dose of curcumin in the form of a 150μL bolus injection. It is note worthy that the curcumin solution prepared for injection was formulated in the same manner as those used for nebulization. Nebulization was performed as outlined in the corresponding methods section.

Prior to sample collection, mice were anesthetized using 2.5% isoflurane at 2 L/min. Whole blood samples (approximately 250μL) were then acquired via cardiocentesis using a 22-guage needle. Once extracted, the needle was removed and each blood sample aliquoted into EDTA-containing or serum-clot tubes for CBC and CP analysis, respectively. Whole blood samples for CBC analysis were kept at 4°C until analysis. In contrast, CP blood samples were allowed to clot at 25°C for 1 h. Following coagulation, serum for CMP analysis was acquired via centrifugation at 3700 g for 20 min at 4°C. Serum samples for CP analysis were stored at 20°C until use.

CBC analysis was performed via an automated hematology instrument. Automated CBC parameters included WBC count, RBC count, HCT, hemoglobin concentration, MCV, MCH, MCHC, and platelet count. Serum samples for CP analysis were transferred into microfuge tubes for clinical chemistry analysis by an automated analyzer.

Statistical analysis

Data was presented as mean ± SD. The comparison between two mice groups (wt versus 5XFAD) was performed by student *t*-test, and for comparing more than two groups (wt, nontreated 5XFAD, treated 5XFAD) we used one-way ANOVA (Prism software). In both cases, the significance was set a 95% of confidence.

For stereological plaque burden quantification, Mann-Whitney-Wilcoxon test is performed on non-treated 5XFAD ($n = 4$, Mdn = 249.5), and treated 5XFAD ($n = 6$, Mdn = 154.5) groups for total plaque count, and in regions: dentate gyrus (DG), stratum (CA), subiculum (sub), and cortex (CTX), respectively. The results are considered significant at a p value <0.05.

RESULTS

Semi-high throughput atomizer device

The aerosol exposure system designed in this work is a prototypical module comprised of a cross-flow atomizer and a control unit used to customize the distributed aerosol flow rate using pressurized air (30 psi) and a liquid pump (Fig. 1B). The aerosol is expelled near the outlet manifold, where it enters the aerosol concentrator chamber under positive pressure. From there, it is distributed equally to 1–5 animals via a delivery trumpet assembled within each nose-only inhalation chamber. The exhaled aerosol is conveyed to an exhaust outlet via escape channels located below the stainless steel delivery port of the nose-only exposure unit. To generate curcumin aerosol, we began by preparing a highly concentrated curcumin formulation (7 mg/mL) using PBS and 10% of tween-20 with the assistance of vigorous stirring at elevated temperature and a sonicator. The materials were then transferred to a calibrated syringe, which was connected securely on a precision pump. For this design, the system can induce inhalable curcumin aerosol to multiple mice simultaneously over the course of several hours for each treatment session.

To compare the brain delivery capacity of inhalable curcumin with other routes, such as I.V. and PO distributions, we tested three cohorts of animals ($n = 3$, each). The data showed that curcumin distribution to the brain via the PO route is ineffective, as our data indicate that

oral curcumin consumption is the worst of all distribution routes. In fact, the bioavailability of curcumin in the brain via PO administration is a mere 0.1% of the treated dose, which is tenfold and twenty-six-fold less effective compared to the I.V. and inhalation routes, respectively (Supplementary Figure 1).

Aerosolized curcumin treatment improves cognitive function

To test the early prevention therapeutic hypothesis, three cohorts of age-matched, six-week-old mice ($n = 10$, each) were assessed, including untreated wt mice, untreated 5XFAD, and 5XFAD mice exposed to aerosolized curcumin. The treated animals were respiratory exposed chronically (54 doses), each time 5 mg/Kg dose of curcumin over the course of four and a half months. Based on our experience and that of others, six-week-old 5XFAD mice express from none to a minimal amount of Aβ plaques in the brain [24, 25]. When the animals reached to 4–6 months of age, however, an abundance of Aβ plaque has accumulated, particularly in the hippocampus, cortex, and subiculum [26]. Thus, six-week-old mice offer an appropriate age window with which to test our AD preventive hypothesis.

We assessed the cognitive function of animals using two iterations of the Y-maze paradigm. The apparatus consists of three arms made of transparent plastics, which merge at the junction to form a Y-shape with the arms at a 120° angle from each other. The walls of the arms were 8–10 cm high, which allowed the mice to see the distal spatial spaces ahead. Each arm is marked with distinct and nonthreatening patterns to provide intra-maze cues to enhance the animals' innate curiosity for a new arm upon reaching the junction without causing stress or affecting the animals' behavior due to reinforcing effects (Supplementary Figure 2). Prior to testing, rigorous control experiments, including arm exploration, new arm entry, and dwell activity were run on all animal cohorts to ensure no intrinsic preference for a particular arm (Supplementary Figure 3). Further, to eliminate possible effects of restraint on behavior, all animals, including the untreated wt and 5XFAD mice, were restrained in the animal holder for the same length of time as those on the atomizer module. The data showed that untreated wt and respiratory curcumin-exposed 5XFAD mice performed at nearly the same level (Fig. 2A). In contrast, we noted a somewhat awkward and disorganized movement among the untreated 5XFAD mice; a finding consistent with cognitive impairment. In fact, the untreated 5XFAD mice were obviously less active, not well groomed and tended to move in one direction, circling several rounds per minute. In comparison, the curcumin-treated 5XFAD mice were more inquisitive and active. They were well groomed and tended to explore the surrounding environment (data not shown). Quantitatively, the percentage of alternation (± SD) among the control and respiratory exposed mice were 76% ± 6.3 and 71% ± 7.5, respectively, versus 53% ± 10.0 for the untreated 5XFAD ($p < 0.0001$).

One week after working memory test, animals were evaluated for the spatial memory test using the same Y-shaped maze. As expected, wt mice entered the novel arms with high frequency and with significant dwelling times. The percentage of time spent by the wt mice exploring the novel arms is approximately 55% ± 7.0 (Fig. 2B). The 5XFAD mice treated chronically with aerosolized curcumin also performed at nearly the same level (48 ± 10.2). In stark contrast, the untreated 5XFAD mice showed a markedly reduced exploring cue for

the novel arm and remained in the novel arms only briefly. The percentage of time spent by the animals in this group exploring the novel arms is approximately 25% ± 9.3. The statistical comparisons between the cohorts were significant ($p < 0.0001$) using one-way ANOVA.

Apparent inhibition of plaque aggregation after longitudinal curcumin inhalation

After a four-and-a half-month therapy, cardiac perfusion was performed on all cohorts of animals using the procedure we described previously [25, 27]. Then, sagittal brain sections were prepared from frozen blocks and stained with 1% thioflavin. The fluorescence signal associated with Aβ plaque expression was assessed using fluorescence microscopy at critical areas such as the hippocampus and subiculum using the GFP channel. As anticipated, no fluorescence signal was detected in wt mice (Fig. 2C). While some degree of fluorescence signal intensity associated with Aβ plaque was detected in the CA1 and subiculum of the curcumin-treated mice (Fig. 2E); however, that expression was unequivocally less intense compared to the untreated 5XFAD counterparts (Fig. 2D). For each individual region of interest, such as CA1 and CA3 and the subiculum and cortical regions, an in-house program developed within MATLAB was used to assess the quantity of Aβ plaque burden across a defined region, including their density and interplaque distance. Quantitatively, after inhaling curcumin from a young age, the amount of Aβ plaque expression in the subiculum and hippocampus regions of maturing animals was reduced by approximately 80% ($p = 0.026$) and 90% ($p = 0.009$), respectively (Fig. 2F). Similar trends were observed in regard to the plaque density in a given region of interest. Among treated animals, there was an apparent reduction in plaque density equivalent to 95% ($p = 0.02$) and 80% ($p = 0.02$) for the subiculum and hippocampus regions, respectively (Fig. 2G). As a result, the percentage of plaque fraction in the subiculum and hippocampus also reduced significantly in the treated animal cohort (Fig. 2H). As a consequence of reduction of plaque burden, the distance between plaque colonies increased (Fig. 2I). Western blot analysis of the brains of curcumin-treated 5XFAD showed a marked reduction of Aβ expression (Fig. 2O). Further, APP expression also attenuated significantly compared to untreated 5XFAD mice (Supplementary Figure 4).

Inhibition of dystrophic neurites and inflammation after curcumin treatment

The data showed that the CA3 region of untreated 5XFAD mice was characterized by an abundance of apparent Aβ plaques and fibrils (Fig. 2J, blue star). Further, we also noted significant dystrophic neurites, exclusively in proximity of the Aβ plaques (Fig. 2J, red discontinuous circles). The neurite autophagic accumulations observed in the TEM data resulted in pigmented structures due to the incompletely digested material from the autophagic vacuoles (Fig. 2K, blue discontinuous circles). Among the untreated 5XFAD mice, two populations of neuritic dendrites were found to be expressed in a Gaussian distribution. In particular, the large of these neurite populations are characterized by a less dense distribution with the apex at 4-5 microns, which represented the abnormal and swollen neurites associated with Aβ pathogenesis (Fig. 2L). In contrast to the untreated animals, the curcumin-treated mice did not exhibit Aβ plaques in the CA3 region (Fig. 2M). There were virtually no dystrophic neurites in the curcumin-treated mice, and the normal neurites are 10-fold smaller than the dystrophic counterpart (Fig. 2N).

To examine the implication of inflammation on the pathogenesis of Aβ, we performed quantitative PCR analysis of COX2 among 5XFAD mice of different ages. Data from this work demonstrated that the expression of COX2 was elevated with the age of the animals and coincides with the temporal accumulation of Aβ burden (Supplementary Figure 5). This observation coincides with the fact that plaque was also expressed significantly among older animals. Therefore, we believe it is worthwhile to ascertain whether the reduced plaque burden in curcumin-treated mice would also correlate to neutralizing COX2-associated inflammation. Western blot analysis of the untreated 5XFAD mice suggest that is the case, as evidenced by the strong expression of COX2 in the brains of those animals. However, chronic respiratory exposure to curcumin not only reduces Aβ expression, but also reduces COX2 expression (Fig. 2O).

Inhalable curcumin is nontoxic

We performed trichrome staining of the lungs to examine collagen deposition or any pathological sign of fibrosis. Three cohorts of age-matched animals were tested in this experiment ($n = 2$, each). The first group involved untreated 5XFAD mice while the second group was acutely exposed to inhalable curcumin, such that animals received a single 6 mg/Kg dose of respired curcumin. The third cohort of mice (chronic) was also treated with inhalable curcumin, but the course was expanded to 54 doses over a 4 and a half month period. After the therapy, the lungs were removed for H&E and trichrome staining, and the data were blindly interpreted by a certified pathologist. At the time of evaluation, acute or chronic inhalation of curcumin produced no detectable collagen deposition or recruitment of inflammatory mediators. In fact, the lungs of both treated animal cohorts were indistinguishable from untreated control mice (Fig. 3A–C). Further, airway epithelium and epithelium in the alveoli appeared normal (data not shown). The lung interstitium and bronchioles in the treated groups were as healthy as those in the untreated group (Fig. 3D), suggesting chronic respiratory exposure to curcumin is safe.

Next, we examined the systemic toxicity of the compounds *in vivo*. In this study, we compared the blood chemistry and hematology of the untreated control mice to the mice via I.V. and respiratory exposure. Blood samples from the different cohorts of animals were collected via cardiocentesis and aliquoted into EDTA-containing or serum-clot tubes for complete blood count and CP analysis, respectively. As shown in Tables 1 and 2, no adverse effects were observed based on the level of curcumin administered, which was 5 mg/Kg for both I.V. and inhalation. When comparing the blood biochemical parameters of mice treated with inhalable curcumin, most of the analytes from curcumin-treated mice are either identical or closed to the values obtained from the untreated control group. We noted some fluctuations in alkaline phosphates and aspartate aminotransferase when animals inhaled or injected with curcumin, respectively. However, those differences were within the standard range. Aside from that issue, all other blood parameters of the inhalable curcumin groups corresponded with the control group. Additionally, the blood hematologic parameters of the inhalable curcumin-treated mice agreed with the control, and necropsy revealed no visible curcumin-induced changes in the animals.

DISCUSSION

In this 18-week preventive therapy, we examined the benefit of longitudinal exposure to curcumin aerosol as a strategy to prevent Aβ buildup in the brain. The data showed that treating young 5XFAD mice with curcumin over the course of their maturation to adulthood improved cognitive function to nearly the same capacity as the control wt mice. Our observation reiterates the data enumerated by Cole et al., which demonstrated that treating APPsw mice with even a small dose of curcumin can lead to a significant reduction of plaque burden in the order of 43–50% in the brains [28]. The versatile application of curcumin is apparent since that work used a different mouse model of AD and reported the distribution of curcumin via I.V. injection. In a recent publication, we noted that the bioavailability of curcumin in the brains of treated mice is nearly the same, regardless of whether curcumin is delivered via inhalation or I.V. administration [23]. However, we also demonstrated that delivery of curcumin via inhalation offers more advantages than I.V. injection, especially when the hippocampal area is the intended destination [23]. The mechanism for delivery to the brain via olfactory pathways has been reported in the past [29, 30]. Aerosol inhalation indeed accomplished a partial distribution of the materials to the olfactory epithelium, the projection of which spans the entire extent of the entorhinal cortex [31, 32]. Further, the entorhinal cortex gives rise to an extension that terminates in the subiculum and the hippocampus [33].

Notably, for this 5XFAD mouse model, the Aβ plaque deposition first started in the subiculum, was more advanced in the early onset of AD compared to those observed in the hippocampal region. Our data are consistent with recent reports, which show the geospatial significance of the subiculum in the early onset of AD [26, 34]. The subiculum serves as the major output structure of the hippocampal formation to widespread subcortical and cortical areas [35]. In AD patients, the subiculum is among the earliest regions to display severe atrophy and pathology [36, 37]. Overall, the use of the 5XFAD mice to test inhalable curcumin represent perfectly useful model with which to validate the efficacy of respiratory exposure to curcumin.

In this work, we also observed that treating 5XFAD mice with curcumin can prevent dystrophic neurites and inflammation from happening. While the striking implication of Aβ plaques in neuron degeneration has been observed and reported in a large number of previous studies [38, 39], there are no reports that describe whether early Aβ plaque pathogenesis affects neurons. Among the key observations we made during this TEM imaging process is the apparent existence of numerous dystrophic neurites in the vicinity of the plaques in untreated 5XFAD mice. In contrast, curcumin-treated counterparts do not express dystrophic neurites. Thus, the neurites in the brains of treated mice are much smaller than those found in untreated animals. What we have not done and wish to pursue in the future is to examine whether this process is reversible. Further, due to the constraints imposed by the narrow field-of-view associated with electron microscopy, we were unable to examine this phenomenon in larger anatomical areas of the brain. With the emergence of noninvasive, high-resolution imaging technologies, the enlarged dendrites might have implications for the early detection and progress monitoring of AD.

Cognizant that degenerating tissue and the deposition of highly insoluble abnormal materials are classical stimulants of inflammation [40], we sought to investigate whether inhalable curcumin also modulates this component of the AD pathological cascade. A large body of literature indicates that during the early onset of AD, damaged neurons and dystrophic neurites coupled with the deposition of insoluble Aβ and neurofibrillary tangles provide the stimuli for inflammation, which may exacerbate the disease [40–42]. Postmortem analysis has shown that NSAIDs can reduce the inflammation that is found consistently in AD brain tissue [43]. Our data suggest that habitual inhaling of curcumin can clear inflammation and plaques simultaneously.

At this stage, we have compelling evidence that inhalable curcumin administered during early stage disease can dramatically reduce the plaque burden and improve memory in a preclinical mouse model. To confirm the extent of plaque clearance shown in thioflavin staining data (Fig. 2), we used immunohistological and stereological techniques to quantify plaque burden of the consecutive slides and this data corroborated with the fluorescence data. Quantitative total plaque burden in untreated 5XFAD mice was significantly higher than treated counterpart determined by Mann-Whitney-Wilcoxon statistical test ($p = 0.0381$) (Fig. 4). Plaque burden was larger in regions DG ($p = 0.0095$), CA ($p = 0.0095$), and Sub ($p = 0.0191$). While cortical plaque burden in treated 5XFAD mice did show a decrease compared non-treated mice (Mdn = 86 and Mdn = 78, respectively). However, the difference was not statistically significant ($p = 0.8$) (Supplementary Table 1).

The clinical applicability of aerosolized curcumin for the treatment or prevention of AD largely relies on the safety of inhaling curcumin. Among the potential concerns to be considered using this method is that the presence of curcumin mist in the lungs may alter their permeability. Further, aerosolized materials may induce fluid accumulation in the alveoli, thus causing damage to the lung epithelium. In particular, the chronic and progressive dysregulation of vascular remodeling may lead to tissue stiffness and fibrosis. However, trichrome staining showed that inhalable curcumin is safe in animals even when exposed to the materials over long periods. While we have not assessed the toxicity of curcumin when administered via other routes, a large body of literature indicated that oral curcumin consumption by rats is safe at a low dose (13.6 mmol/Kg body weight) [44]. At high dose (100 mg/Kg) however, the rats can suffer gastric ulcerations, inflammation, and hyperplasia of the forestomach, cecum and colon [45, 46].

In summary, we have introduced a simple, yet robust technique, quite distinct from conventional approaches, to deliver curcumin to the brain for the potential treatment of AD. The advantage of this technique is its significantly reduced toxicity, since it bypasses the first pass effect. As a result, it reduced degradation of the compound by P450 enzymes. Aside from circulatory distribution, we anticipate that the aerosol can be distributed to the brain by bypassing the BBB through the olfactory epithelium system. Based on the data obtained, we observed that curcumin has a variety of effects, which include decreasing Aβ plaques, reducing the degradation of neurons and imparting an anti-inflammatory effect. The combination of these remarkably improved the overall cognitive function of the preclinical mouse model. Although we tested the technique in a preclinical mouse model, we believe it

is suitable for clinical translation, where consideration of efficacy and toxicity are both pivotal.

Supplementary Material

Refer to Web version on PubMed Central for supplementary material.

Acknowledgments

This work was partially supported by an R01CA16700 (W.P.) from the National Institutes of Health, the VICC Cancer Center Support grant (W.P.) and the National Center for Research Resources, Grant UL1 RR024975-01, and is now at the National Center for Advancing Translational Sciences, Grant 2 UL1 TR000445-06 and the Vanderbilt-Ingram Cancer Center Thoracic Program Initiative. All behavioral testing was undertaken in the Vanderbilt Murine Neurobehavioral Laboratory of the Vanderbilt University Medical Center. Whole slide imaging was performed in the Digital Histology Shared Resources at Vanderbilt University Medical Center.

References

1. Ramos-Rodriguez JJ, Pacheco-Herrero M, Thyssen D, Murillo-Carretero MI, Berrocoso E, Spires-Jones TL, Bacskai BJ, Garcia-Alloza M. Rapid beta-amyloid deposition and cognitive impairment after cholinergic denervation in APP/PS1 mice. J Neuropathol Exp Neurol. 2013; 72:272–285. [PubMed: 23481704]
2. Irvine GB, El-Agnaf OM, Shankar GM, Walsh DM. Protein aggregation in the brain: The molecular basis for Alzheimer's and Parkinson's diseases. Mol Med. 2008; 14:451–464. [PubMed: 18368143]
3. Selkoe DJ. Alzheimer's disease. Cold Spring Harb Perspect Biol. 2011; 3:1–16.
4. Pardridge WM. Alzheimer's disease drug development and the problem of the blood-brain barrier. Alzheimers Dement. 2009; 5:427–432. [PubMed: 19751922]
5. Jones NS, Quraishi S, Mason JD. The nasal delivery of systemic drugs. Int J Clin Pract. 1997; 51:308–311. [PubMed: 9489091]
6. McMartin C, Hutchinson LE, Hyde R, Peters GE. Analysis of structural requirements for the absorption of drugs and macromolecules from the nasal cavity. J Pharm Sci. 1987; 76:535–540. [PubMed: 2889824]
7. Ghosh S, Banerjee S, Sil PC. The beneficial role of curcumin on inflammation, diabetes and neurodegenerative disease: A recent update. Food Chem Toxicol. 2015; 83:111–124. [PubMed: 26066364]
8. Parada E, Buendia I, Navarro E, Avendano C, Egea J, Lopez MG. Microglial HO-1 induction by curcumin provides antioxidant, anti-neuroinflammatory and glioprotective effects. Mol Nutr Food Res. 2015; 59:1690–1700. [PubMed: 26047311]
9. Sandersen C, Bienzle D, Cerri S, Franck T, Derochette S, Neven P, Mouytis-Mickalad A, Serteyn D. Effect of inhaled hydrosoluble curcumin on inflammatory markers in broncho-alveolar lavage fluid of horses with LPS-induced lung neutrophilia. Multidiscip Respir Med. 2015; 10:16. [PubMed: 25908974]
10. Santos AM, Lopes T, Oleastro M, Gato IV, Floch P, Benejat L, Chaves P, Pereira T, Seixas E, Machado J, Guerreiro AS. Curcumin inhibits gastric inflammation induced by Helicobacter pylori infection in a mouse model. Nutrients. 2015; 7:306–320. [PubMed: 25569625]
11. Galaly SR, Ahmed OM, Mahmoud AM. Thymoquinone and curcumin prevent gentamicin-induced liver injury by attenuating oxidative stress, inflammation and apoptosis. J Physiol Pharmacol. 2014; 65:823–832. [PubMed: 25554986]
12. Rashid K, Sil PC. Curcumin enhances recovery of pancreatic islets from cellular stress induced inflammation and apoptosis in diabetic rats. Toxicol Appl Pharmacol. 2015; 282:297–310. [PubMed: 25541178]
13. Das L, Vinayak M. Long term effect of curcumin in restoration of tumour suppressor p53 and phase-II antioxidant enzymes via activation of Nrf2 signalling and modulation of inflammation in prevention of cancer. PLoS One. 2015; 10:e0124000. [PubMed: 25860911]

14. Das L, Vinayak M. Curcumin attenuates carcinogenesis by down regulating proinflammatory cytokine interleukin-1 (IL-1alpha and IL-1beta) via modulation of AP-1 and NF-IL6 in lymphoma bearing mice. Int Immunopharmacol. 2014; 20:141–147. [PubMed: 24613204]
15. Das L, Vinayak M. Anti-carcinogenic action of curcumin by activation of antioxidant defence system and inhibition of NF-kappaB signalling in lymphoma-bearing mice. Biosci Rep. 2012; 32:161–170. [PubMed: 21831045]
16. Loch-Neckel G, Santos-Bubniak L, Mazzarino L, Jacques AV, Moccelin B, Santos-Silva MC, Lemos-Senna E. Orally administered chitosan-coated polycaprolactone nanoparticles containing curcumin attenuate metastatic melanoma in the lungs. J Pharm Sci. 2015; 104:3524–3534. [PubMed: 26085173]
17. Mancarella S, Greco V, Baldassarre F, Vergara D, Maffia M, Leporatti S. Polymer-coated magnetic nanoparticles for curcumin delivery to cancer cells. Macromol Biosci. 2015; 15:1365–1374. [PubMed: 26085082]
18. Parashar G, Capalash N. Promoter methylation-independent reactivation of PAX1 by curcumin and resveratrol is mediated by UHRF1. Clin Exp Med. 2016; 16:471–478. [PubMed: 26081871]
19. Ahmad MZ, Alkahtani SA, Akhter S, Ahmad FJ, Ahmad J, Akhtar MS, Mohsin N, Abdel-Wahab BA. Progress in nanotechnology-based drug carrier in designing of curcumin nanomedicines for cancer therapy: Current state-of-the-art. J Drug Target. 2016; 24:273–293. [PubMed: 26066739]
20. Endo H, Nikaido Y, Nakadate M, Ise S, Konno H. Structure activity relationship study of curcumin analogues toward the amyloid-beta aggregation inhibitor. Bioorg Med Chem Lett. 2014; 24:5621–5626. [PubMed: 25467149]
21. Maiti P, Manna J, Veleri S, Frautschy S. Molecular chaperone dysfunction in neurodegenerative diseases and effects of curcumin. Biomed Res Int. 2014; 2014:495091. [PubMed: 25386560]
22. Malar DS, Devi KP. Dietary polyphenols for treatment of Alzheimer's disease–future research and development. Curr Pharm Biotechnol. 2014; 15:330–342. [PubMed: 25312617]
23. McClure R, Yanagisawa D, Stec D, Abdollahian D, Koktysh D, Xhillari D, Jaeger R, Stanwood G, Chekmenev E, Tooyama I, Gore JC, Pham W. Inhalable curcumin: Offering the potential for translation to imaging and treatment of Alzheimer's disease. J Alzheimers Dis. 2015; 44:283–295. [PubMed: 25227316]
24. Eimer WA, Vassar R. Neuron loss in the 5XFAD mouse model of Alzheimer's disease correlates with intraneuronal Abeta42 accumulation and Caspase-3 activation. Mol Neurodegener. 2013; 8:2. [PubMed: 23316765]
25. McClure RA, Chumbley CW, Reyzer ML, Wilson K, Caprioli RM, Gore JC, Pham W. Identification of promethazine as an amyloid-binding molecule using a fluorescence high-throughput assay and MALDI imaging mass spectrometry. Neuroimage Clin. 2013; 2:620–629. [PubMed: 24179813]
26. Oakley H, Cole SL, Logan S, Maus E, Shao P, Craft J, Guillozet-Bongaarts A, Ohno M, Disterhoft J, Van Eldik L, Berry R, Vassar R. Intraneuronal beta-amyloid aggregates, neurodegeneration, and neuron loss in transgenic mice with five familial Alzheimer's disease mutations: Potential factors in amyloid plaque formation. J Neurosci. 2006; 26:10129–10140. [PubMed: 17021169]
27. Pham W, Zhao BQ, Lo EH, Medarova Z, Rosen B, Moore A. Crossing the blood-brain barrier: A potential application of myristoylated polyarginine for in vivo neuroimaging. Neuroimage. 2005; 28:287–292. [PubMed: 16040255]
28. Lim GP, Chu T, Yang F, Beech W, Frautschy SA, Cole GM. The curry spice curcumin reduces oxidative damage and amyloid pathology in an Alzheimer transgenic mouse. J Neurosci. 2001; 21:8370–8377. [PubMed: 11606625]
29. Tjalve H, Henriksson J, Tallkvist J, Larsson BS, Lindquist NG. Uptake of manganese and cadmium from the nasal mucosa into the central nervous system via olfactory pathways in rats. Pharmacol Toxicol. 1996; 79:347–356. [PubMed: 9000264]
30. Witter MP, Amaral DG. Entorhinal cortex of the monkey: V. Projections to the dentate gyrus, hippocampus, and subicular complex. J Comp Neurol. 1991; 307:437–459. [PubMed: 1713237]
31. Price JL. An autoradiographic study of complementary laminar patterns of termination of afferent fibers to the olfactory cortex. J Comp Neurol. 1973; 150:87–108. [PubMed: 4722147]

32. Insausti R, Marcos P, Arroyo-Jimenez MM, Blaizot X, Martinez-Marcos A. Comparative aspects of the olfactory portion of the entorhinal cortex and its projection to the hippocampus in rodents, nonhuman primates, and the human brain. Brain Res Bull. 2002; 57:557–560. [PubMed: 11923028]
33. van Groen T, Miettinen P, Kadish I. The entorhinal cortex of the mouse: Organization of the projection to the hippocampal formation. Hippocampus. 2003; 13:133–149. [PubMed: 12625464]
34. Trujillo-Estrada L, Davila JC, Sanchez-Mejias E, Sanchez-Varo R, Gomez-Arboledas A, Vizuete M, Vitorica J, Gutier-rez A. Early neuronal loss and axonal/presynaptic damage is associated with accelerated amyloid-beta accumulation in AbetaPP/PS1 Alzheimer's disease mice subiculum. J Alzheimers Dis. 2014; 42:521–541. [PubMed: 24927710]
35. Ding SL. Comparative anatomy of the prosubiculum, subiculum, presubiculum, postsubiculum, and parasubiculum in human, monkey, and roden. J Comp Neurol. 2013; 521:4145–4162. [PubMed: 23839777]
36. Davies CA, Mann DM, Sumpter PQ, Yates PO. A quantitative morphometric analysis of the neuronal and synaptic content of the frontal and temporal cortex in patients with Alzheimer's disease. J Neurol Sci. 1987; 78:151–164. [PubMed: 3572454]
37. Simic G, Kostovic I, Winblad B, Bogdanovic N. Volume and number of neurons of the human hippocampal formation in normal aging and Alzheimer's disease. J Comp Neurol. 1997; 379:482–494. [PubMed: 9067838]
38. Quinn J, Davis F, Woodward WR, Eckenstein F. Beta-amyloid plaques induce neuritic dystrophy of nitric oxide-producing neurons in a transgenic mouse model of Alzheimer's disease. Exp Neurol. 2001; 168:203–212. [PubMed: 11259108]
39. Brendza RP, Bacskai BJ, Cirrito JR, Simmons KA, Skoch JM, Klunk WE, Mathis CA, Bales KR, Paul SM, Hyman BT, Holtzman DM. Anti-Abeta antibody treatment promotes the rapid recovery of amyloid-associated neuritic dystrophy in PDAPP transgenic mice. J Clin Invest. 2005; 115:428–433. [PubMed: 15668737]
40. Akiyama H, Barger S, Barnum S, Bradt B, Bauer J, Cole GM, Cooper NR, Eikelenboom P, Emmerling M, Fiebich BL, Finch CE, Frautschy S, Griffin WS, Hampel H, Hull M, Landreth G, Lue L, Mrak R, Mackenzie IR, McGeer PL, O'Banion MK, Pachter J, Pasinetti G, Plata-Salaman C, Rogers J, Rydel R, Shen Y, Streit W, Strohmeyer R, Tooyoma I, Van Muiswinkel FL, Veerhuis R, Walker D, Webster S, Wegrzyniak B, Wenk G, Wyss-Coray T. Inflammation and Alzheimer's disease. Neurobiol Aging. 2000; 21:383–421. [PubMed: 10858586]
41. Kitazawa M, Oddo S, Yamasaki TR, Green KN, LaFerla FM. Lipopolysaccharide-induced inflammation exacerbates tau pathology by a cyclin-dependent kinase 5-mediated pathway in a transgenic model of Alzheimer's disease. J Neurosci. 2005; 25:8843–8853. [PubMed: 16192374]
42. McGeer EG, McGeer PL. The importance of inflammatory mechanisms in Alzheimer disease. Exp Gerontol. 1998; 33:371–378. [PubMed: 9762518]
43. Mackenzie IR. Postmortem studies of the effect of anti-inflammatory drugs on Alzheimer-type pathology and associated with inflamation. Neurobiol Aging. 2001; 22:819–822. [PubMed: 11754988]
44. Wahlstrom B, Blennow G. A study on the fate of curcumin in the rat. Acta Pharmacol Toxicol (Copenh). 1978; 43:86–92. [PubMed: 696348]
45. Kelloff GJ, Crowell JA, Hawk ET, Steele VE, Lubet RA, Boone CW, Covey JM, Doody LA, Omenn GS, Greenwald P, Hong WK, Parkinson DR, Bagheri D, Baxter GT, Blunden M, Doeltz MK, Eisenhauer KM, Johnson K, Knapp GG, Longfellow DG, Malone WF, Nayfield SG, Seifried HE, Swall LM, Sigman CC. Strategy and planning for chemopreventive drug development: Clinical development plans II. J Cell Biochem Suppl. 1996; 26:54–71. [PubMed: 9154168]
46. Gupta B, Kulshrestha VK, Srivastava RK, Prasad DN. Mechanisms of curcumin induced gastric ulcer in rats. Indian J Med Res. 1980; 71:806–814. [PubMed: 7409877]

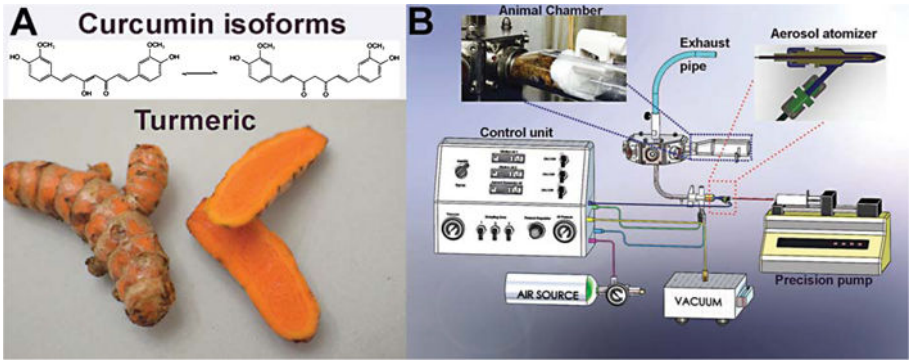

Fig. 1.

A) The chemical structure of curcumin, a key compound in the turmeric root, which is used in several types of oriental food and traditional medicine. This natural product exists as an equilibrium form between enol and ketone isomers. B) Overall design of an innovative, prototype benchtop aerosol generator that produces curcumin aerosols for inhalation therapy. It produces polydisperse aerosols by atomizing a solution. The aerosol particle concentration can be adjusted by changing the flow of the compressed air on the control unit. The air is then expanded through the atomizer nozzle and produces a high-velocity jet. As a result of the decreased static pressure under Bernoulli's law, the liquid curcumin solution is drawn from the precision pump. Instantaneously, a high-velocity airflow smashes the solution into a droplet aerosol in the flow, which then is conveyed into a chamber. With the current design, the chamber can accommodate five animals, which inhale the aerosols via tapered nose cones attached inside the restraint holder. The chamber has another channel that redirects exhaled air to the system's exhaust, thus rebreathing of exhaled air is prevented.

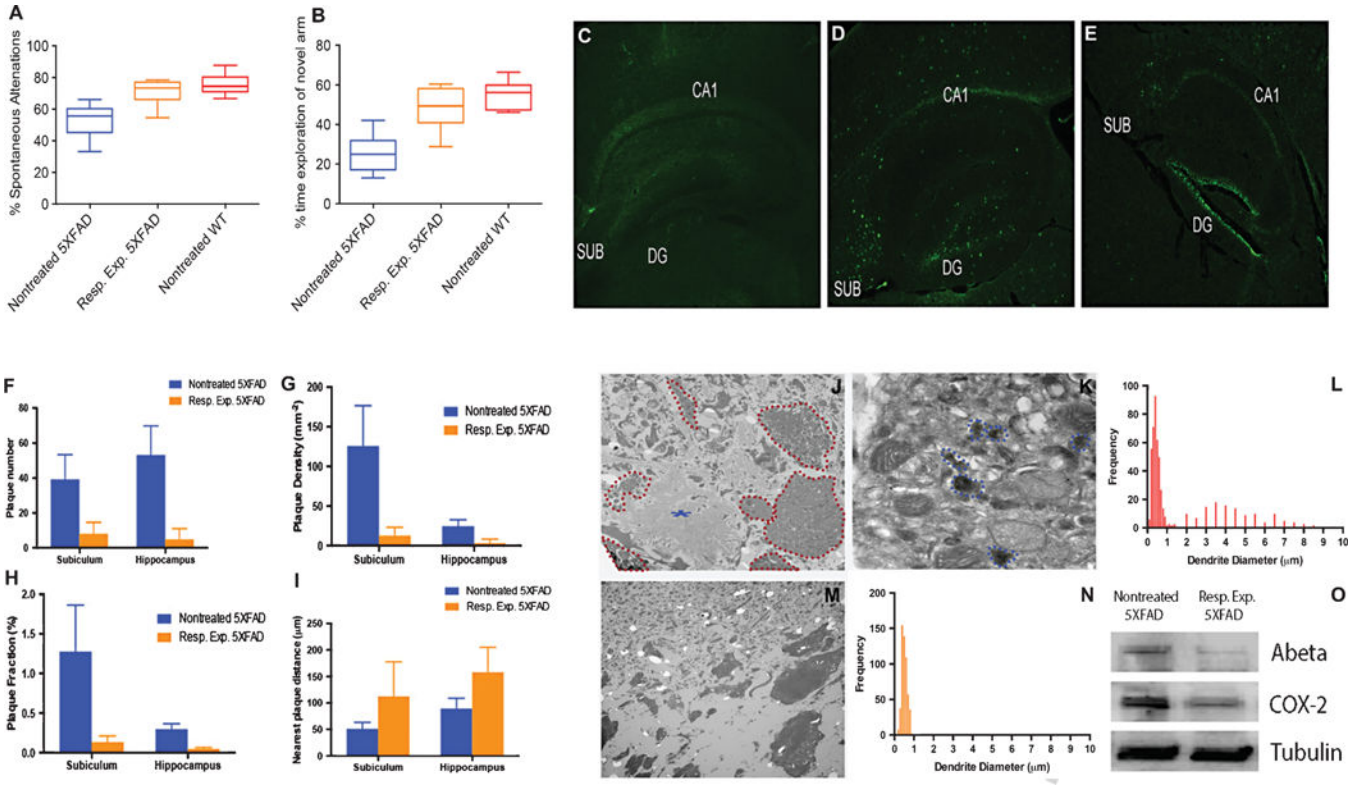

Fig. 2.

Improved hippocampal learning and memory in 5XFAD mice correlates with reduced Aβ expression. A) Assessment of the working memory of three cohorts of animals, including untreated 5XFAD, respiratory curcumin-exposed 5XFAD (12 × 5 mg/Kg) and untreated wt mice ($n = 10$, each) using a Y-shaped maze ($p < 0.0001$, one-way ANOVA). B) A two-trial Y-shaped maze was used to test the spatial memory of the animal cohorts noted in (A). The effect of the curcumin after 4 months of inhalation therapy (7 mg/mL, × 12) on spatial memory following 6 min of Y-maze exploration. Each bar represents mean ± SD, statistical significant differences ($p < 0.0001$, one-way ANOVA). C–E) Thioflavin T staining of sagittal brain sections, particularly in the hippocampus region, dentate gyrus (DG) and subiculum (SUB) of 5-month-old untreated wt mice (C), untreated 5XFAD (D), and 5XFAD mice exposed via the respiratory system (E). F) The number of plaques in the subiculum and hippocampus in untreated 5XFAD versus their respiratory exposed counterparts ($p < 0.05$). G) Density of plaques defined as number of plaques per mm^2 in the subiculum or hippocampus. H) Plaque fraction defined as the plaque occupancy of plaque in a defined area multiplied by 100. I) Distance between plaques in the region of interest. J) Ultrastructural analysis of the CA3 sub region of the hippocampus of the untreated 5XFAD mice. An electron microscopy micrograph of a large Aβ plaque (asterisk). The data also showed that the plaque is surrounded by swollen dystrophic neurites (dotted red lines). K) The dystrophic neurites of the CA3 of untreated mice are filled with autophagic vesicles that contain amorphous and electron-dense materials (dotted blue lines). L) Gaussian distribution curve of two populations of dendrite diameters observed in untreated 5XFAD mice. M) No detectable Aβ plaques were noted in the CA3 region of the curcumin-respiratory-treated

5XFAD mice. N) No swollen neurites were detected, therefore, only one population of neurites exists in a normal physiological size. O) Western blot analysis of A protein and COX2 expression. All tissues were normalized to β -tubulin. ($p < 0.05$ for A and $p < 0.05$ for COX2).

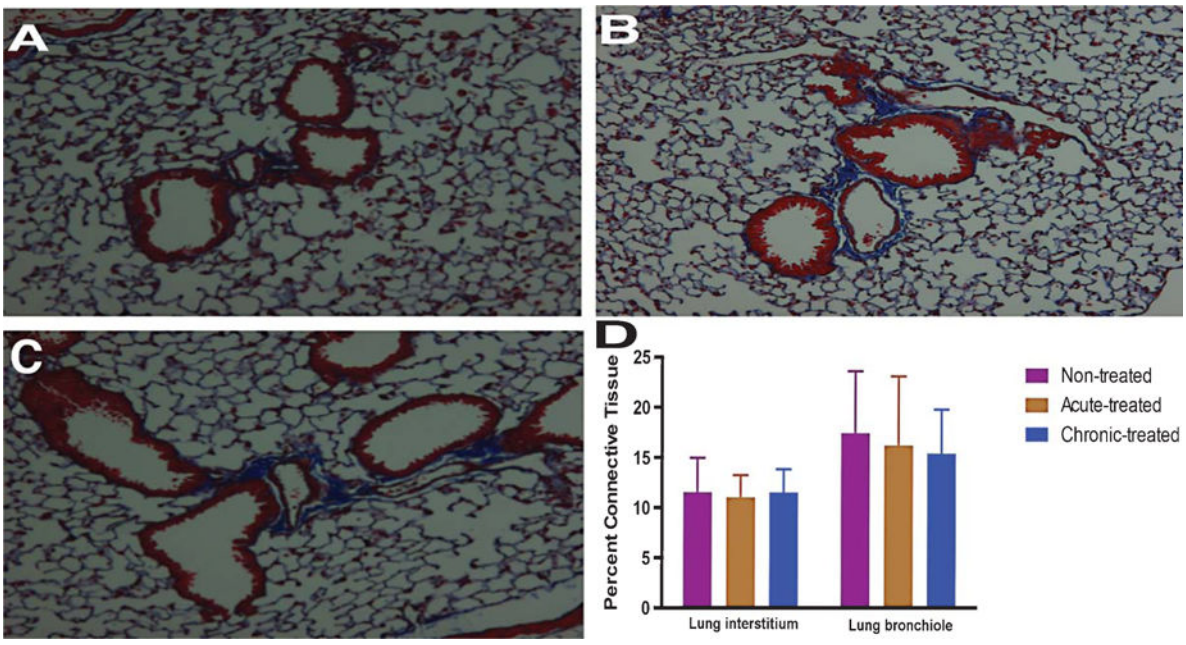

Fig. 3.

Pulmonic toxicity effects of chronic versus longitudinal exposure to curcumin in 6-month-old 5XFAD mice. A) Masson's trichrome staining of the lungs of untreated animals. B) acutely treated (5 mg/Kg) and (C) chronically treated (54 × 5 mg/Kg) curcumin inhalation (n = 3, each). D) Quantification of collagen deposition in the respiratory bronchioles and interstitial pulmonary tissues. Data were quantified from trichrome stained sections (n = 30 per group) using image-J.

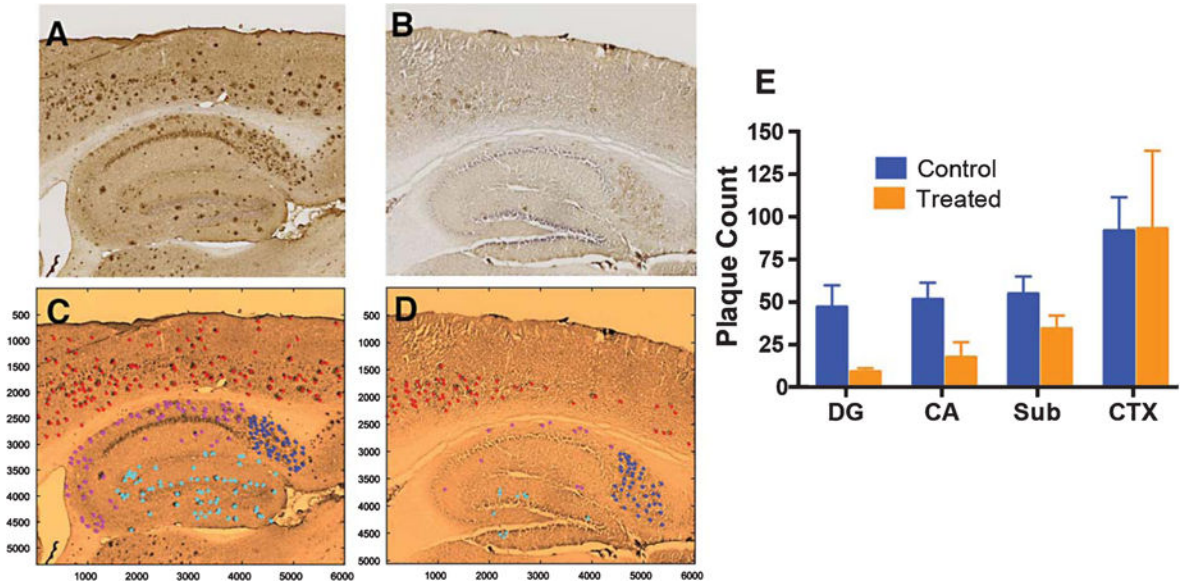

Fig. 4.

Immunohistological and stereological information to quantify plaque burden in 5XFAD mice. These brain slides are consecutive sections obtained from animals described in Fig. 2. (A, C) nontreated mice; (B, D) treated mice. C and D are false-colored version of A and B, respectively. Plaque count of each region of the brain was distinguished by color: DG (Cyan), CA (Magenta), Sub (Blue), and CTX (red). The total plaque burden and regional burden in DG, CA, and Sub in untreated 5XFAD was significantly higher versus their respiratory exposed counterparts ($p = 0.0381$, $p = 0.0095$, $p = 0.0095$, and $p = 0.0191$, respectively).

Table 1

Blood chemistry

Blood chemistry	Resp. Exp.	I.V.	Nontreated control	Normal range
Na (mmol/L)	146.1	139.7	151	147–167
K (mmol/L)	5.75	3.56	6.7	5–9
Cl (mmol/L)	116.1	122.3	108	104–120
ALP (U/L)	50	103	80	44–118
ALT (U/L)	88	42.5	61	26–120
AST (U/L)	114	195.5	173	69–191
BUN (mg/dL)	35	37	33	19–34
Creatinine (mg/dL)	0.5	0.5	0.5	0.5–0.8

ALP, alkaline phosphates; ALT, alanine aminotransferase; AST, aspartate aminotransferase; BUN, blood urea nitrogen.

Table 2

Complete blood count

	Resp. Exp.	I.V.	Nontreated control
WBC	6.57	9.43	6
HCT	40.0	40.2	41.6
RBC	9.1	6.8	9.8
HB	12.4	9.3	13.1
MCV	43.8	44.1	42.6
MCH	13.7	13.5	13.4
MCHC	31.3	30.7	31.5
RDW	13.3	13.7	14.4
RSD	5.8	6.1	6.1
RETIC	33.1	22.9	48.8
RETIC %	0.6	0.3	0.5
PLT	737.5	994.5	1058.5